Principal curvature effects on the early evolution of three-dimensional single-mode Richtmyer-Meshkov instabilities

Xisheng Luo, Ben Guan, Zhigang Zhai, and Ting Si*

Advanced Propulsion Laboratory, Department of Modern Mechanics, University of Science and Technology of China, Hefei 230026, China

(Received 28 November 2015; revised manuscript received 21 January 2016; published 18 February 2016)

The Richtmyer-Meshkov instability (RMI) of single-mode air-SF_6 interfaces is studied numerically and the emphasis is placed on the effect of the principal curvature on the early evolution of the shocked interface. Two three-dimensional initial interfaces with opposite (3D−) and identical (3D+) principal curvatures and a traditional two-dimensional interface (2D) are considered. The weighted essentially nonoscillatory scheme and the Level-Set method combined with the real ghost fluid method are adopted. For comparison, perturbations on the initial interfaces with the same wavelength and amplitude in the symmetry plane are employed. The numerical results confirm the experimental finding that the growth rate of perturbations in the symmetry plane at the linear stage in the 3D− case is much smaller than that in the 2D and 3D+ cases. The difference among them can be ascribed to the different pressure and vorticity distributions associated with the principal curvatures of the initial interface. On the one hand, the high-pressure zones in the vicinity of the deformed interface are significantly different for three cases especially in the very beginning. The shock convergence and divergence at the interface are more severe in the 3D+ case than those in the 2D case, while the wave pattern in the 3D− case is more complex. On the other hand, the baroclinic vorticity distribution plays a leading role in the interface deformation of the 3D RMI after the passage of the planar shock. The accumulated vorticity changes the movement of the deformed interface and makes the local growth of perturbations different among three cases.

DOI: 10.1103/PhysRevE.93.023110

I. INTRODUCTION

The Richtmyer-Meshkov instability (RMI) occurs when an initially perturbed density interface between two different fluids is accelerated by a shock wave. The interface is compressed in the beginning of the shock-interface interaction and develops gradually due to the baroclinic vorticity caused by the misalignment between the pressure and the density gradients at the interface. In a planar shock case, the perturbation of the interface grows linearly with time in the early stage, as first predicted theoretically by Richtmyer [1] and confirmed experimentally by Meshkov [2]. In contrast, in the late stage, the growth of the perturbation becomes nonlinear with spikes and bubbles of the interface evolving asymmetrically and finally turns into turbulent mixing. Extensive studies have been performed on the subject of RMI and significant advancements have been achieved by experiments, theories, and simulations [3,4] due to the significant applications in fields such as inertial confinement fusion [5], supernova explosions [6], and supersonic combustion [7].

In previous studies, the shapes of the initial interface mainly include spherical and cylindrical bubbles [4,8], polygonal gaseous cylinders [9,10], and single-mode and multimode interfaces [11–14]. The single-mode gaseous interface is one of the most used cases due to its simple geometry and sinusoidal structure. As shown in Fig. 1, there are three typical configurations depending on the principal curvatures of the initial single-mode interface, including a two-dimensional interface with only one principal curvature (2D), a three-dimensional interface with two identical principal curvatures (3D+), and a three-dimensional interface with two opposite principal curvatures (3D−) in the transverse and longitudinal directions. The 2D interface has been widely used in the study of the RMI to model the growth rate of the mixing layer in the linear, nonlinear, and turbulent regimes [15,16], while studies of the 3D+ interface [17–19] and the 3D− interface [20] are still in their early stages. The 3D RMI cases leave some open questions; in particular the stability characteristics of a surface bent in the transverse and the longitudinal directions are not fully understood yet [21]. Moreover, in most applications the RMI occurs generally in 3D geometric conditions and the development of a density interface is intrinsically in the 3D behavior. Therefore, it is still desirable to put forth great effort in studying the 3D cases in order to understand the properties of the 3D RMI, even for the early evolution stages.

A minimum-surface featured single-mode interface can be recognized as one of the 3D− interfaces, which has a zero mean curvature with opposite principle curvatures at every point of the interface [22]. In our previous work, we generated this type of 3D− interface by soap film techniques and performed RMI experiments in a shock tube [20]. A 3D stability analysis was also carried out to propose an extended theoretical model that combined the early linear growth with the late-time nonlinear growth for the whole evolution process of the 3D− configuration. The experimental and theoretical investigations indicated that the growth rate of the mixing layer at the symmetric plane in the 3D− case was much slower than the 3D+ and 2D counterparts. However, due to the limitations of the initial interface formation and the schlieren photography in experiments, it was not possible to observe the dynamic behavior of the 3D− single-mode interface at a very early stage of evolution. Moreover, it was difficult to obtain the quantitative information of the flow field for understanding the vortex dynamics and the shock refraction and reflection in 3D single-mode RMI. The present work is a follow-up of our previous study, aiming to numerically study the effects of principal curvatures on the interface evolution.

*Corresponding author: tsi@ustc.edu.cn

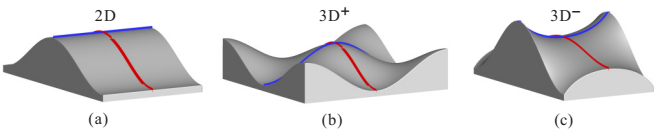

FIG. 1. Schematics of three typical single-mode interfaces with (a) only one principal curvature (2D), (b) identical principal curvatures (3D+), and (c) opposite principal curvatures (3D−) in the transverse and longitudinal directions.

II. NUMERICAL METHOD AND VALIDATION

A. Numerical method and physical model

In the numerical simulation, we will restrict our focus to the early stage of the RMI; therefore, the turbulent mixing is beyond the scope of the present work. The 3D unsteady compressible Euler equations with the ideal gas law as the equation of state are appropriately adopted. The level set method [23] and the real ghost fluid method [24] are used to represent the interface that initially separates the different gases. In a Cartesian coordinate system, the level set function $\phi(x,y,z,t)$ satisfies

$$\frac{\partial \phi}{\partial t} + u\frac{\partial \phi}{\partial x} + v\frac{\partial \phi}{\partial y} + w\frac{\partial \phi}{\partial z} = 0, \tag{1}$$

where (u,v,w) are the velocity components in the x, y, and z directions, respectively. The location of the interface is captured automatically by advancing $\phi(x,y,z,t)$ to the next time step. Reinitialization is used to maintain the level set function as a signed distance function

$$\phi_t + S(\phi_0)\left(\sqrt{\phi_x^2+\phi_y^2+\phi_z^2}-1\right) = 0, \qquad \phi(x,y,z,0) = \phi_0, \tag{2}$$

where the sign function is $S(\phi_0) = \phi_0/\sqrt{\phi_0^2+\Delta l^2}$, with ϕ_0 the location of the interface and Δl the mesh size. The governing equation and the level set function are solved by a fifth-order weighted essentially nonoscillatory scheme [25] in uniform cubic cells and advanced in time by the third-order Runge-Kutta method.

For comparison, Fig. 2 presents the initial setting for the 3D− case based on our previous experimental work [20]. The interface has an initial amplitude of $a_o = 5$ mm at the top and the bottom boundaries (line OR'-OL-OR) and a wavelength of $\lambda = 35$ mm. Based on the property of a minimum surface for the 3D− case [22], the interfacial geometry can be characterized in each xz plane as

$$z = f(y)\cos(kx), \quad y \in [-9,9], \tag{3}$$

and

$$y = \pm\int_{a_i}^{f(y)} \frac{dx}{\sqrt{e^{k^2(x^2-a_i^2)}-1}}, \tag{4}$$

where the plus (minus) sign stands for $y > 0$ ($y < 0$) and a_i for the perturbation amplitude of the symmetry plane at $y = 0$. Considering the initial amplitude $a_o = 5$ mm at the top and the bottom boundaries ($y = \pm 9$ mm), the interfacial amplitude $a_i = 1.79$ mm at the symmetry plane ($y = 0$) can be determined from Eq. (4).

The 2D, 3D+, and 3D− interfaces are considered in the present numerical simulations, in which the computational domains are similar. The interfacial geometries in each xz plane have the mathematical expression for three cases as written in Eq. (3), where $f(y) = a_i$ for the 2D case and $f(y) = a_i\cos(ky)$ for the 3D+ case.

Due to the symmetric structures of the whole physical space shown in Fig. 2, we consider the upper left quarter as the computational domain with a cuboid shape of $17.5 \times 9 \times 100$ mm^3. (The length in the z direction can be adjusted in different numerical cases to improve the efficiency.) The locations of the gaseous interface initially separating SF_6 (right) from air (left) and of the planar shock wave with a Mach number of $M_s = 1.21$ initially moving from left to right along the positive z direction are indicated in Fig. 2. The preshock flow field is set to be stationary and the postshock flow variables are computed by the Rankine-Hugoniot relations. The boundary conditions on the six surfaces of the cuboid include two solid boundaries (top and back surfaces), two symmetric boundaries (bottom and front surfaces) and two outflow boundaries (left and right surfaces). The outflow conditions are enforced on the two surfaces by applying a zeroth-order extrapolation to the boundaries. The effects of the mesh size on the numerical accuracy are evaluated in advance and the number of grid cells is finally considered to be $175 \times 90 \times 1000$, which corresponds to a uniform grid size of $\Delta x = \Delta y = \Delta z = 0.1$ mm.

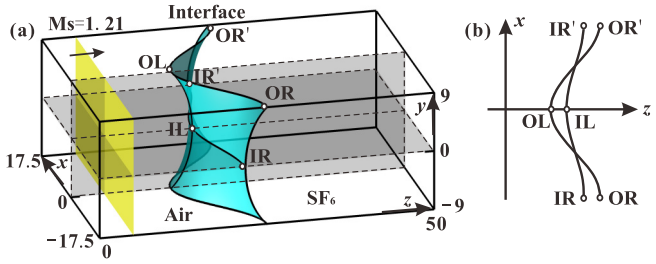

FIG. 2. (a) Initial setting for the 3D− single-mode interface and (b) top view of the interface with IL, IR, IL and OL, OR, OR (I, inner; O, outer; L, left; R, right) denoting the positions of the troughs and crests of the initially perturbed interface at $y = 0$ and 9 mm, respectively.

B. Comparison with previous experiments

The complete evolution processes of the 2D, 3D+, and 3D− interfaces accelerated by the planar shock wave in the early stage have been simulated numerically. In order to validate the numerical method, the results for the 3D− interface case are first compared with previous experimental observations [20]. In the experiment, schlieren photography only records the shock propagation and interface deformation in an integrated view, while in the numerical simulation, the 3D flow structures can be obtained. Figure 3 presents an example of the deformation of an initial 3D− interface with $a_o = 5$ mm, $a_i = 1.79$ mm, and $\lambda = 35$ mm accelerated by a planar shock wave at different moments. It can be easily seen that the 3D numerical simulation is able to provide details of the evolving interface that behaves differently along the

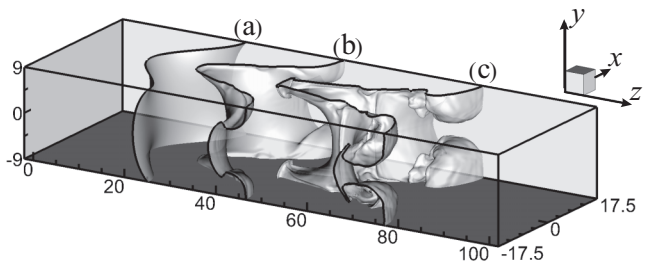

FIG. 3. Numerical simulation of the flow structures for the 3D− interface at different moments: (a) $t = 0$, (b) $t = 0.26$ ms, and (c) $t = 0.61$ ms.

y axis owing to the 3D characteristics. Figure 4 compares the schlieren images of the shocked 3D− interface from the experiments (upper part) with the corresponding numerical results (lower part). Although the schlieren results indicate an integrated view of the deformed interfaces along the y direction at different times, the evolving interfaces in the symmetry ($y = 0$, i.e., IR'-IL-IR in Fig. 2) and boundary ($y = \pm 9$ mm, i.e., OR'-OL-OR in Fig. 2) planes can be easily extracted. Therefore, the interfacial evolution of the symmetry or the top-bottom boundary can be revealed by the inner or outer contours in each image, as represented by the dashed lines in Fig. 4. It can be directly found that the numerical results exhibit all the features of the shock-interface interaction presented in the experiments and good agreement between them can be obtained. Furthermore, Fig. 5 compares the geometric quantities that characterize the evolution of this minimum surface between the experimental (symbols) and the numerical results (lines). The displacements of the crest and the trough along the symmetry plane (the inner contour) are nearly the same between experimental and numerical results. There is a little difference between the outer contour in the numerical simulation and the experimental counterpart, which may lie in the fact that the soap film and the small protrusions for fixing the soap film in experiments never exist in the numerical simulation. The effects of other slight differences including the incident shock strength, the temperature, and the pressure can be neglected. Overall, the agreement between experiments and numerical simulations is acceptable.

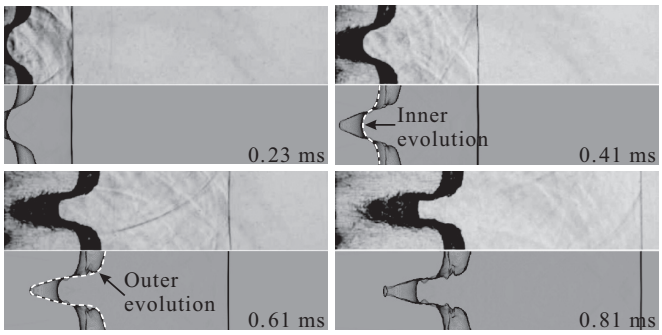

FIG. 4. Schlieren scenarios of the evolution of a minimum-surface featured air-SF_6 interface impacted by a shock wave with $M_s = 1.21$. The top halves are experimental schlieren results and the bottom halves are numerical ones, indicating an integrated view of the deformed interfaces along the y direction at different times.

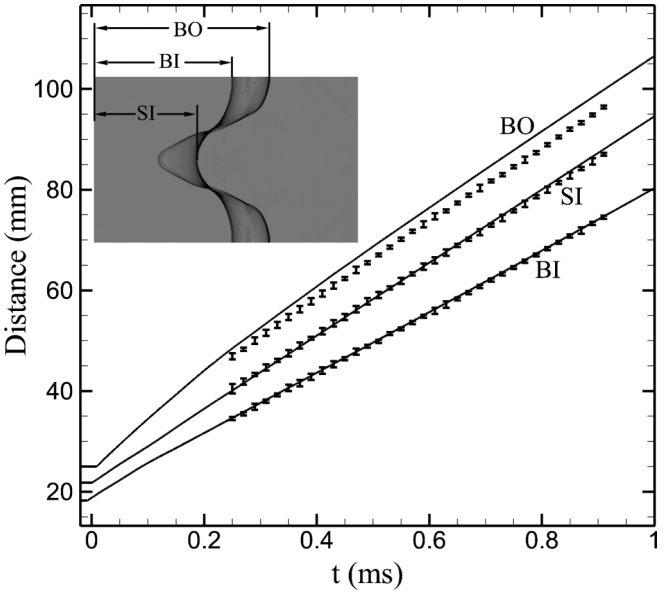

FIG. 5. Comparison of three geometric quantities that characterize the evolution of the shocked 3D− interface between experimental (symbols) and numerical (lines) results. The definitions of the measurement are indicated in the inset image taken from the numerical simulation in Fig. 4.

Previous experimental studies have found that the instability growth rates in the symmetry plane are distinct among the 2D, 3D+, and 3D− single-mode cases in the linear stage [20]. Figure 6 presents the numerical results of the dimensionless growth rates in the $y = 0$ plane for 2D, 3D+, and 3D− single-mode interfaces with the initial wavelength of $\lambda = 35$ mm and amplitude $a_i = 1.79$ mm subjected to a shock wave of $M_s = 1.21$. The quantities are nondimensionalized as $\bar{a} = k(a_i^t - Z_c a_i^0)$ and $\tau = k v_i^{RM}(t - t_0)$, with $v_i^{RM} = Z_c k a_i A^+ \Delta V$ the growth rate estimated from the 2D impulsive model [1], $Z_c = 1 - \Delta V / W_s$ the compression factor, ΔV the velocity jump of the shocked interface, W_s the incident shock velocity, k the wave number, and A^+ the postshock Atwood number. The data are nearly the same as those in the experimental observations, which further validates the numerical method. According to the extended linear theoretical model [20], the growth rate of the 2D interface symmetry plane is v_i^{RM}, for the 3D+ case it is $\sqrt{2} v_i^{RM}$, and for the 3D− case it is $(2 - \sqrt{2}) v_i^{RM}$. It can be seen that the predictions of the theoretical model fit the numerical results well in the linear stage ($\tau < 0.7$). The 3D+ instability grows much faster than the 2D one, while the 3D− instability has the lowest growth rate. This would be ascribed to the different principal curvatures among them. In comparison with the 2D interface instability, the identical principal curvatures of the 3D+ interface enhance the instability, while the opposite principal curvatures of the 3D− interface suppress the instability. At later times, the linear theory overpredicts the growth rates for all three cases because of the nonlinearity caused by the appearance of the bubble-spike structures.

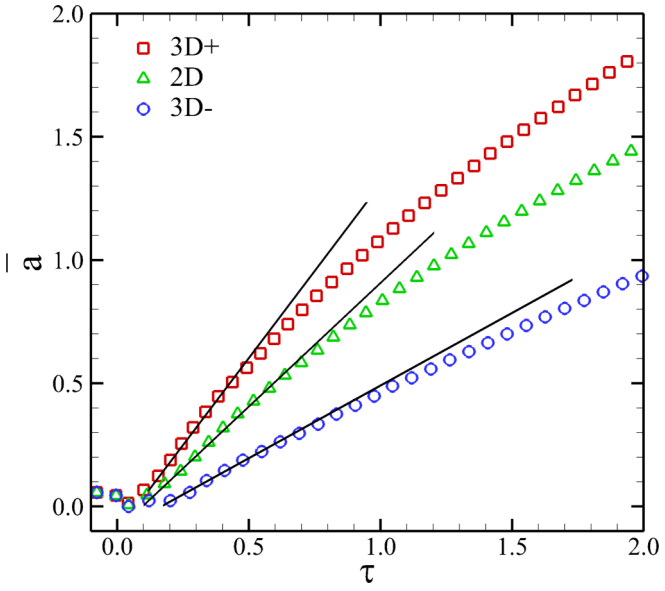

FIG. 6. Dimensionless growth rates in the $y = 0$ plane for 3D−, 3D+, and 2D single-mode interfaces subjected to the planar shock wave of $M_s = 1.21$. The symbols stand for the numerical results and the solid lines for the theoretical ones predicted by the extended impulsive models.

III. PRINCIPAL CURVATURE EFFECTS ON THE INTERFACE EVOLUTION

The effect of the postshock pressure gradients in the vicinity of the interface on the early evolution of the 3D single-mode RMI is assessed numerically. As the previous experiments for the 3D− interface hardly obtain the pressure distribution [20], we first simulate the 3D flow field. Figure 7 presents the high-pressure zones (HPZs) for the shocked 3D− interface at two moments after the shock-interface interactions (i.e., 15.76 and 50.78 μs). When the planar shock impacts the interface, a transmitted shock (TS) and a reflected shock (RS) are formed. The TS moves from left to right and the high-pressure zone HPZ1 can form immediately between the interface and the TS along the middle of the top and bottom walls. The RS moves from right to left and high-pressure zones HPZ2 and HPZ3 arise in the postshock area along the diagonal lines of the RS. As time proceeds, the shapes of the RS and the TS change and the postshock pressure distributions vary in the 3D postshock space. The HPZ3 expands and is further divided into two parts along the x axis and the upper and lower parts around the four corners of HPZ2 move toward the symmetry plane along the y axis. Meanwhile, HPZ1 develops and another HPZ4 arises along the middle of the front and back walls after the passage of the TS. Due to the larger acoustic impedance of SF_6 on the right side of interface, the TS moves more slowly than the RS, and the HPZ1 and the HPZ4 will be maintained for a relatively long time. These HPZs cause pressure drops at two sides of the evolving interface and directly affect the growth of perturbations in the flow field.

Figure 8 further presents schlieren images of the early evolution of the shock pattern and the interface deformation subjected to the shocked 3D− interface at four characteristic slices. It can be seen that the initial opposite interfacial principal curvatures have great effects on the pressure distributions in the flow field, resulting in different shapes of the TS, the RS, and the deformed interface along each slice, respectively. In the symmetry plane (S1) and the top (or bottom) plane (S2), the initial interfaces have a single-mode shape with the same wavelength $\lambda = 35$ mm and different amplitudes $a_i = 1.79$ mm and $a_o = 5$ mm, respectively. For the interface along the top or bottom boundary plane, the HPZ1 enhances the transition of its crests into spikes (e.g., OL in S2 and IL in S3) and the HPZ2 promotes the transition of its troughs into bubbles (e.g., OR in S2 and OR in S4). In contrast, for the interface along the symmetry plane the HPZ3 suppresses the development of its crests into spikes (e.g., IL in S1 and IL in S3) and the HPZ4 suppresses the development of its troughs into bubbles (e.g., IR in S1 and OR in S4). As indicated in Fig. 3, the interfaces along S2 ($y = \pm 9$ mm, i.e., OR'-OL-OR in Fig. 2) develop much faster than that along the S1 ($y = 0$, i.e., IR'-IL-IR in Fig. 2), in which the bubble-spike structures hardly appear in the early stage. It should be mentioned that the opposite principal curvatures along the interface cause 3D structures of the RS and the TS with convergent and divergent characteristics. For example, the RS front shown in S3 can be divided into three parts, including one middle strong convergent part and one upper and one lower weak divergent parts. Because of the strong and weak reflections, rarefaction waves can form at the junctions of different pressure zones, inducing the variation of pressure distributions in the flow field. These phenomena in the 3D− case are much different from those in the 2D [15,16] and 3D+ [17–19] cases.

The evolutions of the 3D+ and 2D shocked interfaces are simulated numerically and further compared with the 3D− case. Figure 9 presents the cross-sectional view of three

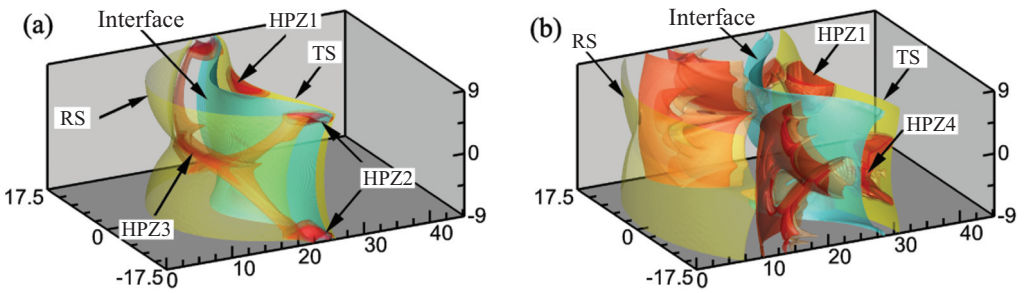

FIG. 7. Distribution of the high-pressure zone (HPZ) for the shocked 3D− interface at two moments: (a) 15.76 μs and (b) 50.78 μs, respectively. RS denotes reflected shock and TS transmitted shock.

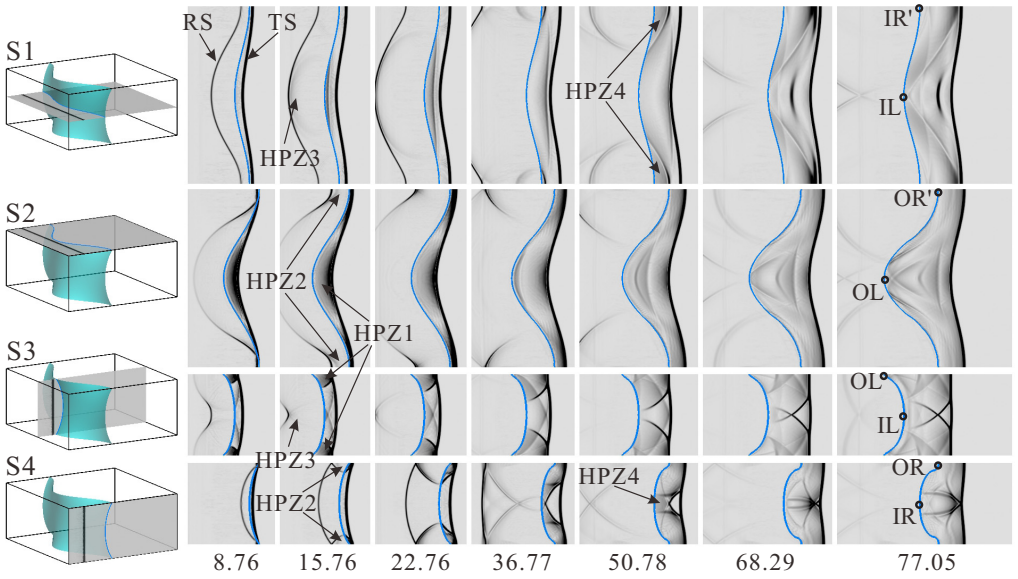

FIG. 8. Cross-sectional view of the numerical schlieren sequences showing the early evolution of the shocked 3D− interface in four characteristic planes at the moments in sequence: 8.76, 15.76, 22.76, 36.77, 50.78, 68.29, and 77.05 μs.

shocked interfaces in the $y = 0$ plane at different moments after the shock-interface interactions, respectively. In the very beginning, the shapes of the TS, the RS, and the shocked interface are nearly the same in the $y = 0$ plane due to the same amplitude of the initial interface and the same shock strength. However, as the principal curvatures are different, the difference of the pressure distributions in the vicinity of the interface will result in different velocities of the interface. Figure 10 plots the pressure distributions along the central line in the $y = 0$ plane for the shocked 3D+, 2D, and 3D− interfaces at 8.76, 15.76, and 22.76 μs, respectively. Since the initial shape of the 3D+ interface is horizontally convex to the negative z direction, the RS is horizontally divergent during its traveling from right to left. Compared with the 2D case, the RS acquires an extra divergent expansion as its initial shape is vertically convex to the negative z direction. Meanwhile, the shock convergence on the right side of the interface caused by the TS is also stronger in the 3D+ case than that in the 2D case. Therefore, the pressure gradient across both sides of the interface in the 3D+ case is higher than that in the 2D case. The

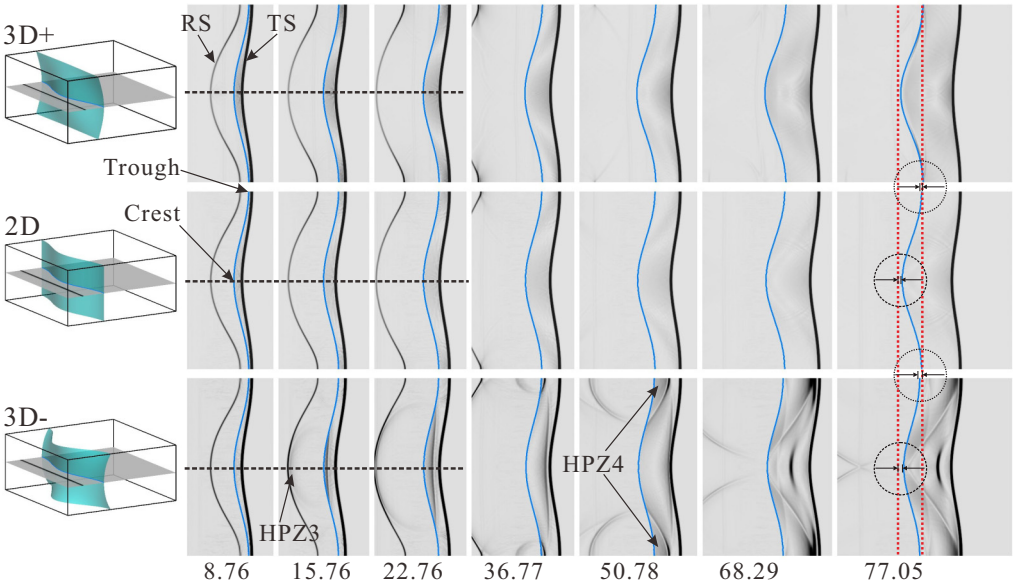

FIG. 9. Comparison of the numerical schlieren sequences among the shocked 3D+, 2D, and 3D− single-mode interfaces showing the early evolution of them in the symmetry plane at different moments in sequence: 8.76, 15.76, 22.76, 36.77, 50.78, 68.29, and 77.05 μs. At the moment 77.05 μs, the locations of the crest and the trough for the three cases are indicated by vertical dashed lines to show the differences of their displacements.

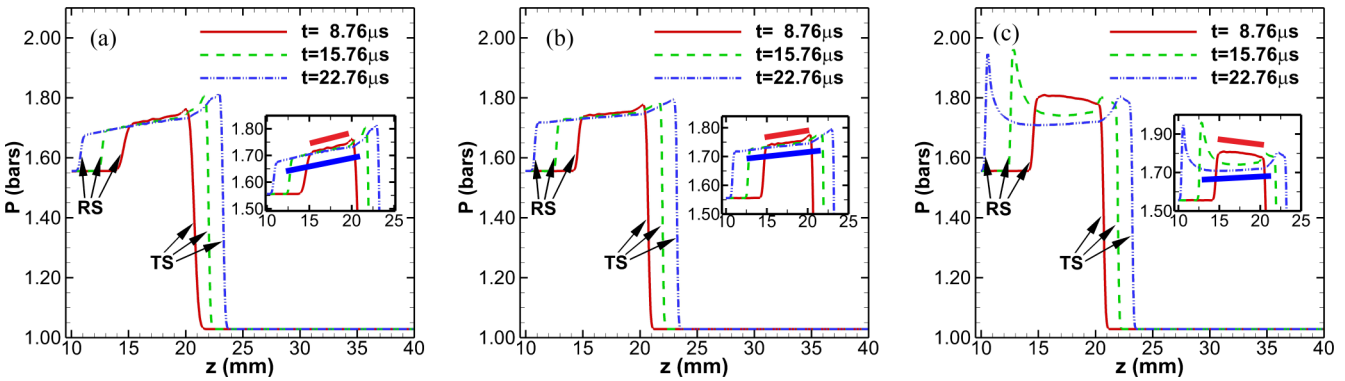

FIG. 10. Pressure distributions along the central line at $y = 0$ plane for the shocked (a) 3D+, (b) 2D, and (c) 3D− interfaces at 8.76, 15.76, and 22.76 μs, respectively. The inset images indicate the pressure gradients in the vicinity of the evolving interface. The pressure data are extracted along the horizontal dashed lines shown in Fig. 9.

wave pattern in the 3D− case is much more complex. Because of the opposite directions of the two principal curvatures, the rarefaction waves appear after the wave convergence of the RS and result in the formation of HPZ3. It can be easily seen that the pressure gradient in the 3D− case at 8.76 μs is even opposite to the pressure gradients in the 2D and 3D+ cases. As a result, the crest of the interface in the 3D− case will move more slowly than that in the 2D case and the 3D+ case will obtain the largest displacement of the interface corresponding to the crest, as indicated in Fig. 9 at 77.05 μs. Moreover, the displacements of the evolving interface corresponding to the trough for three cases follow the same rules. Therefore, the growth rate of perturbations at the linear stage in the 3D− case is much smaller than that in the 2D and 3D+ cases and the 3D+ case has the largest perturbation growth, which firmly confirms the experimental finding [20].

Due to the misalignment of density and pressure gradients, baroclinic vorticity is deposited at the gaseous interface. Figure 11 presents the vorticity distributions in the flow field at 15.76 μs. The 2D vorticity distributions are plotted in three

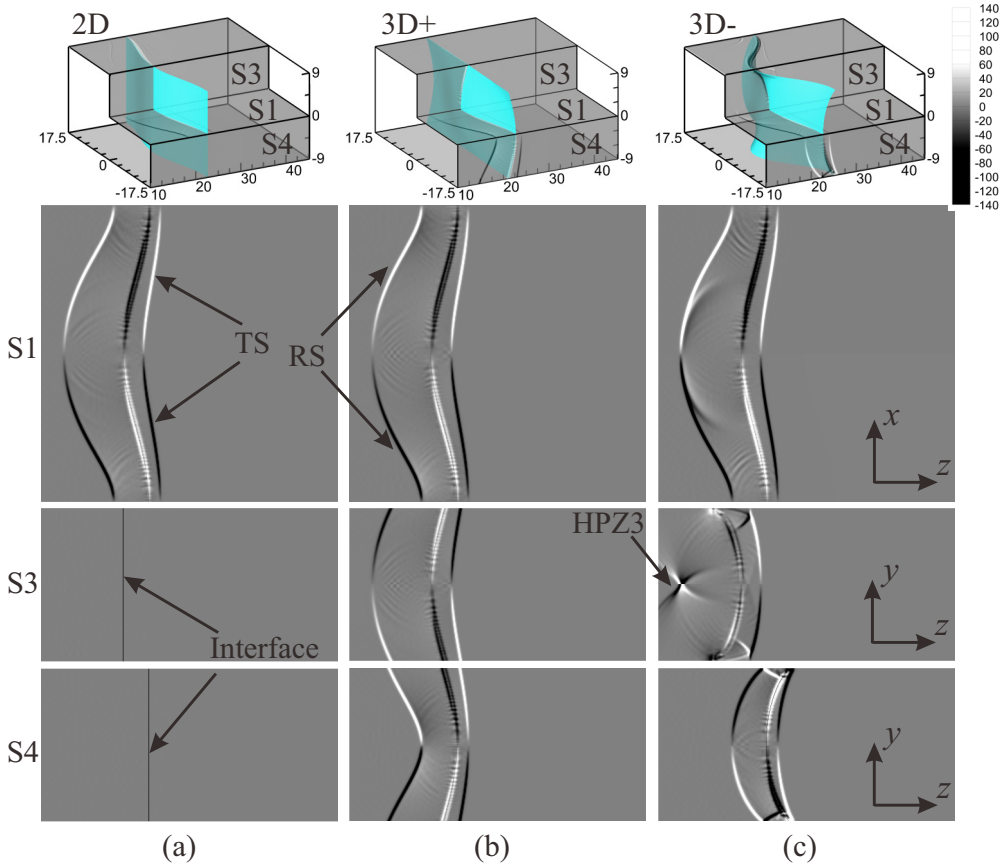

FIG. 11. Vorticity distributions in the flow field for the shocked (a) 2D, (b) 3D+, and (c) 3D− interfaces at 15.76 μs. The definitions of S1, S3, and S4 are indicated in Fig. 8.

characteristic slices where S1, S3, and S4 correspond to the cut planes shown in Fig. 8. In the horizontal symmetry plane S1 ($y = 0$), three cases acquire nearly the same vorticity distributions because of the same initial shock strength and interface shape. The vorticity induces velocities of the interface in the postshock flow field. In the vertical central plane S3 ($x = 0$), however, there are great differences among three cases. Considering the top half part of the interface, one can obtain that the vorticity is equal to zero in the 2D case, positive in the 3D+ case, and negative in the 3D− case. The same direction of the vorticity deposited on the 3D+ interface around its crest will intensify the instability growth, which is much larger than that in the 2D case, while the opposite direction of the vorticity deposited on the 3D− interface around its crest will suppress the instability growth. Meanwhile, the interface trough (S4) experiences nearly the same tendency of movements due to the deposited vorticity. As time proceeds, the accumulated vorticity will further change the flow field and make the phenomena among three cases much more different.

IV. CONCLUSION

This numerical work has explored the effects of initial interfacial principal curvatures on the early evolution of the 3D RMI. Three types of single-mode air-SF_6 interface (i.e., 2D, 3D+, and 3D−) accelerated by a planar shock are considered. Specifically, the initial interfaces have perturbations of the same wavelength and amplitude in the symmetry plane, but their principal curvatures are completely different. Compared with the 2D case, identical principal curvatures in the 3D+ case can increase the local growth of perturbations, while the opposite principal curvatures in the 3D− case can reduce the local growth. In the very beginning (e.g., 8.76 μs in Fig. 9), the shock reflection and transmission cause different pressure gradients across the interface for three cases. The pressure gradient in the 3D− case is even opposite to the pressure gradients in 2D and 3D+ cases (e.g., Fig. 10). The vorticity distributions are further given to assess the difference among three cases. In particular, in the vertical central plane (i.e., S3 in Fig. 11), there is no vorticity in the 2D case and the vorticity directions are just opposite in the 3D+ and 3D− cases. The numerical results can confirm our previous experimental findings and validate the theoretical model for the 3D RMI [20]. It is conjectured that the 3D RMI could be suppressed or retarded to some extent by a clever design of the initial shape of the interface.

ACKNOWLEDGMENTS

This work was supported by the National Natural Science Foundation of China (Grants No. 11302219, No. 11272308, and No. NSAF U1530103).

[1] R. D. Richtmyer, Commun. Pure Appl. Math. **13**, 297 (1960).
[2] E. E. Meshkov, Fluid Dyn. **4**, 101 (1969).
[3] M. Brouillette, Annu. Rev. Fluid Mech. **34**, 445 (2002).
[4] D. Ranjan, J. Oakley, and R. Bonazza, Annu. Rev. Fluid Mech. **43**, 117 (2011).
[5] D. L. Lindl, R. L. McCrory, and E. M. Campbell, Phys. Today **45**(9), 32 (1992).
[6] W. D. Arnett, J. N. Bahcall, R. P. Kirshner, and S. E. Woosley, Annu. Rev. Astron. Astrophys. **27**, 629 (1989).
[7] F. Marble, G. Hendricks, and E. Zukoski, *Proceedings of the 23rd AIAA, SAE, ASME, and ASEE Joint Propulsion Conference, San Diego, 1987* (American Institute of Aeronautics and Astronautics, New York, 1987), pp. 1–8.
[8] J. F. Haas and B. Sturtevant, J. Fluid Mech. **181**, 41 (1987).
[9] Z. Zhai, M. Wang, T. Si, and X. Luo, J. Fluid Mech. **757**, 800 (2014).
[10] X. Luo, M. Wang, T. Si, and Z. Zhai, J. Fluid Mech. **773**, 366 (2015).
[11] A. Rikanati, D. Oron, O. Sadot, and D. Shvarts, Phys. Rev. E **67**, 026307 (2003).
[12] C. Mariani, M. Vandenboomgaerde, G. Jourdan, D. Souffland, and L. Houas, Phys. Rev. Lett. **100**, 254503 (2008).
[13] G. C. Orlicz, B. J. C. Balakumar, C. D. Tomkins, and K. P. Prestridge, Phys. Fluids **21**, 064102 (2009).
[14] S. Balasubramanian, G. C. Orlicz, B. J. C. Balakumar, and K. P. Prestridge, Phys. Fluids **24**, 034103 (2012).
[15] M. Latini, O. Schilling, and W. S. Don, Phys. Fluids **19**, 024104 (2007).
[16] K. O. Mikaelian, Phys. Rev. E **79**, 065303(R) (2009).
[17] P. R. Chapman and J. W. Jacobs, Phys. Fluids **18**, 074101 (2006).
[18] C. C. Long, V. V. Krivets, J. A. Greenough, and J. W. Jacobs, Phys. Fluids **21**, 114104 (2009).
[19] E. Leinov, G. Malamud, Y. Elbaz, L. A. Levin, G. Ben-Dor, D. Shvarts, and O. Sadot, J. Fluid Mech. **626**, 449 (2009).
[20] X. Luo, X. Wang, and T. Si, J. Fluid Mech. **722**, R2 (2013).
[21] R. Krechetnikov, J. Fluid Mech. **625**, 387 (2009).
[22] C. Isenberg, *The Science of Soap Films and Soap Bubbles* (Dover, New York, 1992).
[23] S. Osher and J. A. Sethian, J. Comput. Phys. **79**, 12 (1988).
[24] C. W. Wang, T. G. Liu, and B. C. Khoo, SIAM J. Sci. Comput. **28**, 278 (2006).
[25] G. Jiang and C. Shu, J. Comput. Phys. **126**, 202 (1996).